Materials Today Bio 26 (2024) 101111

Contents lists available at ScienceDirect

Materials Today Bio

journal homepage: www.journals.elsevier.com/materials-today-bio

Establishing stable and highly osteogenic hiPSC-derived MSCs for 3D-printed bone graft through microenvironment modulation by CHIR99021-treated osteocytes

Qiuling Guo [a], Jingjing Chen [a], Qiqi Bu [a], Jinling Zhang [a], Minjie Ruan [a], Xiaoyu Chen [b], Mingming Zhao [b], Xiaolin Tu [a,**], Chengzhu Zhao [a,*]

[a] *Laboratory of Skeletal Development and Regeneration, Key Laboratory of Clinical Laboratory Diagnostics (Ministry of Education), College of Laboratory Medicine, Chongqing Medical University, Chongqing, 400016, China*

[b] *Center for Medical Epigenetics, School of Basic Medical Sciences, Chongqing Medical University, Chongqing 400016, China*

A R T I C L E I N F O

Keywords:
Human induced pluripotent stem cell
Mesenchymal stem cell
Osteogenic microenvironment
3D bioprinting
Wnt signalling

A B S T R A C T

Human induced pluripotent stem cell (hiPSC)-derived mesenchymal stem cells (iMSCs) are ideal candidates for the production of standardised and scalable bioengineered bone grafts. However, stable induction and osteogenic differentiation of iMSCs pose challenges in the industry. We developed a precise differentiation method to produce homogeneous and fully differentiated iMSCs. In this study, we established a standardised system to prepare iMSCs with increased osteogenic potential and improved bioactivity by introducing a CHIR99021 (C91)-treated osteogenic microenvironment (COOME). COOME enhances the osteogenic differentiation and mineralisation of iMSCs via canonical Wnt signalling. Global transcriptome analysis and co-culturing experiments indicated that COOME increased the pro-angiogenesis/neurogenesis activity of iMSCs. The superior osteogenic differentiation and mineralisation abilities of COOME-treated iMSCs were also confirmed in a Bio3D module generated using a polycaprolactone (PCL) and cell-integrated 3D printing (PCI3D) system, which is the closest model to *in vivo* research. This COOME-treated iMSCs differentiation system offers a new perspective for generating highly osteogenic, bioactive, and anatomically matched grafts for clinical applications.

Statement of significance: Although human induced pluripotent stem cell-derived MSCs (iMSCs) are ideal seed cells for synthetic bone implants, the challenges of stable induction and osteogenic differentiation hinder their clinical application. This study established a standardised system for the scalable preparation of iMSCs with improved osteogenic potential by combining our precise iMSC differentiation method with the CHIR99021 (C91)-treated osteocyte osteogenic microenvironment (COOME) through the activation of canonical Wnt signalling. Moreover, COOME upregulated the pro-angiogenic and pro-neurogenic capacities of iMSCs, which are crucial for the integration of implanted bone grafts. The superior osteogenic ability of COOME-treated iMSCs was confirmed in Bio3D modules generated using PCL and cell-integrated 3D printing systems, highlighting their functional potential *in vivo*. This study contributes to tissue engineering by providing insights into the functional differentiation of iMSCs for bone regeneration.

1. Introduction

Bone defects are prevalent clinical injuries, with over 4 million patients undergoing bone transplantation or alternative surgical treatments annually [1]. Synthetic implants play a vital role in treating bone defects because of their versatility, offering patients convenient and tailored therapeutic options while avoiding the complications associated with traditional autologous bone grafts. Despite their benefits, integration challenges at the transplantation site may arise due to limited biocompatibility, often requiring revision within 5–20 years [2–4]. Therefore, optimising artificial bone grafts to achieve high bioactivity is crucial to meet clinical demands. Human bone marrow mesenchymal stem cells (hBMSCs), known for their accessibility, biological activity, and osteogenic capacity, are the primary choice of seed cells for

* Corresponding author.
** Corresponding author.
E-mail addresses: xtu@cqmu.edu.cn (X. Tu), chengzhu.zhao@cqmu.edu.cn (C. Zhao).

https://doi.org/10.1016/j.mtbio.2024.101111
Received 24 February 2024; Received in revised form 17 May 2024; Accepted 31 May 2024
Available online 1 June 2024

bioengineered bone development [5–7]. However, challenges arise owing to variations in the quality and potency of hBMSCs derived from different donors. Human induced pluripotent stem cell (hiPSC)-derived mesenchymal stem cells (iMSCs) have the potential to address these concerns. Given their unlimited self-renewal capacity and pluripotency, iPSCs are well suited for the standardised and scalable production of bone graft materials [8–12].

hiPSCs offer a unique advantage in regenerative medicine owing to their accessibility and ability to avoid ethical concerns [13]. Research involving the transplantation of hiPSC-derived cells to treat Parkinson's disease [14], spinal cord injuries [15], macular degeneration [16] and more has reached clinical phase I and II trials. These advancements assure for translational applications of hiPSC-derived cells. However, there is a lack of research on clinical trials of bone diseases using iMSCs. The primary challenge lies in achieving a precise and controlled differentiation system for iMSCs for large, stable regenerative applications. To date, iMSCs have mostly been prepared through the embryoid body step or immediately induced by signalling molecules and growth factors (one-step method), likely resulting in an inconsistent and heterogeneous iMSC cell population [17–19]. To address this challenge, we previously developed an effective two-step iMSC induction method by mimicking the embryonic development process. This approach generates iMSCs through the neural crest cell (NCC) lineage using a chemically defined medium (CDM) containing minimal chemical signalling inhibitors and growth factors. This differentiation method generates induced NCCs (iNCCs) that can be consistently passaged while maintaining typical marker expression and differentiation capability [8,20–22]. This approach enables the creation of large-scale frozen stocks of homogeneous, fully differentiated iMSCs suitable for standardised production and clinical applications.

Current approaches for applying hBMSCs or iMSCs to bone defects often fail to achieve the desired osteogenic potential [23–26]. Mainstream methods to enhance the osteogenic capacity of MSC-containing bone implants involve utilising bone matrix composite materials, such as hydroxyapatite and tricalcium phosphate [27–29] or incorporating growth factors and regulatory proteins into bone implants [30,31]. However, these methods have limitations due to their potential side effects and insufficient bioactivity. Additionally, challenges in maintaining a stable microenvironment over an extended period after transplantation may affect sustained osteogenesis, highlighting the need to optimise the microenvironment of MSC-containing artificial bone grafts to promote successful bone regeneration.

Osteocytes play a pivotal role in providing a fundamental microenvironment that influences the activities of osteoblasts and osteoclasts via mechanosensation and signal transduction [32,33]. Our previous investigations have elucidated that activation of the Wnt/β-catenin signalling pathway in osteocytes is crucial for mediating the metabolic effects on bone synthesis [34,35]. In addition, *in vitro* activation of canonical Wnt signalling in osteocytes forms an effective osteogenic microenvironment that enhances osteoblast differentiation of ST2 cells [36,37] In this study, using a specific and safe Wnt agonist, CHIR99021 (C91), we investigated the contribution of the C91-treated osteogenic microenvironment (COOME) to the osteogenic differentiation of iMSCs. In addition, using our previously developed polycaprolactone (PCL) and cell-integrated 3D printing (PCI3D) system [38], which supports cell growth in shape-specific scaffolds by providing a suitable pore size for nutrient transport and excretion, we constructed COOME-containing PCI3D modules to imitate *in vivo* environments. This approach enabled the evaluation of the bone regeneration potential of COOME-iMSCs. Furthermore, we confirmed the superior effect of COOME-iMSC on angiogenesis and neurogenesis.

This study proposes a novel approach wherein the osteogenic microenvironment directs the iMSC fate towards osteoblastic differentiation, offering a potential strategy for the scalable production of biologically active bone graft materials.

2. Materials and methods

2.1. Cells and reagents

The hiPSC line (DYR0100, derived from the foreskin fibroblast cell line SCRC-1041) was purchased from ATCC (Manassas, VA, USA). Murine MLO-Y4 osteocyte-like cells were kindly provided by Professor Lynda Bonewald of the Indian University School of Medicine. Human umbilical vein endothelial cells (HUVECs) and human neuroblastoma cells (SH-SY5Y) were purchased from ATCC.

C91, SB431542, and iCRT-14 were purchased from MedChem Express (Monmouth Junction, NJ, USA). Lyophilised gelatin methacryloyl (GelMA) and the photocrosslinking agent (LAP) were sourced from Sunp Biotech (Beijing, China). PCL was purchased from Aladdin (Shanghai, China).

Assay Kits: BCIP/NBT alkaline phosphatase (AP) colour rendering and AP activity assay kits, modified Oil Red O Staining Kit, alizarin red S staining kit, live/dead viability assay kit, and nuclear and cytoplasmic protein extraction kit were obtained from Beyotime Biotechnology (Shanghai, China). Alcian blue 8GX Solution was from OriCell (Guangzhou, China), and the Cell Counting Kit-8 (CCK-8) assay kit was from Biosharp (Hefei, China).

2.2. Derivation of iMSCs from iPSCs

hiPSCs were first differentiated into iNCCs using a slightly modified version of a well-established method to generate iMSCs [39]. Briefly, hiPSCs were seeded onto PSCeasy-coated plates at a density of 5×10^3 cells/cm^2 in Pluripotency Growth Master 1 (PGM1) medium (Cellapy, Beijing, China). iNCCs were induced in a chemically defined medium (CDM) [39] supplemented with 10 μM SB431542 and 1 μM C91 for 10–12 days. CD271$^+$ iNCC were then sorted using fluorescence-activated cell sorting (FACS) and expanded onto fibronectin (Millipore, Bedford, USA)-coated plates at a density of 6.5×10^4 cell/cm^2 in CDM supplemented with 10 μM SB431542, 10 ng/mL recombinant human EGF (R&D Systems, Minneapolis, USA) and 10 ng/mL recombinant human bFGF (Absin, Shanghai, China). A flow cytometry caliber instrument (BD Biosciences, LSR II, USA) and BD Diva software version 6.1.3 were used for FAC sorting and data analysis.

After 4–5 passages, the medium of iNCCs was replaced with αMEM supplemented with 10 % FBS (Biological Industries, Kibbutz Beit Haemek, Israel) and 10 ng/mL bFGF. Cells started showing morphological changes after 6 h. At this stage, the cells were identified as iMSCs (passage 0). Weekly passages were then performed using 0.25 % trypsin-EDTA at a density of 1×10^4 cells/cm^2. Subsequent experiments typically used iMSCs from passages 3–5.

2.3. Three lineage differentiation of iMSCs

Osteogenic differentiation: A total of 1×10^5 iMSCs per well were seeded on a 12-well plate and cultured in osteogenic medium containing DMEM, 100 nM dexamethasone, 10 mM β-glycerophosphate disodium salt solution, and 50 μg/mL L-ascorbic acid 2-(dihydrogen phosphate) magnesium salt (AA2P) for 21 days [35]. Matrix mineralisation was analysed using alizarin red S staining.

Adipogenic differentiation: 4×10^5 iMSCs were seeded on a 12-well plate and cultured in adipogenic medium containing α-MEM, 0.5 μM hydrocortisone, 0.5 mM IBMX, and 60 μM indomethacin. Lipid droplets were observed microscopically after 7 days of culture. The cells were fixed with 4 % formalin for 5 min at room temperature, then washed three times with double distilled water, stained with a modified Oil Red O staining kit following instructions, and photographed under a microscope.

Chondrogenic differentiation: iMSCs were induced to differentiate using an OriCell Mesenchymal Stem Cell Chondrogenic Differentiation Kit (Cyagen Biosciences) following the manufacturer's instructions.

Briefly, 3×10^5 cells were centrifuged to form a cell pellet and cultured in a chondrogenic differentiation medium for 2 weeks. The pellets were formalin-fixed for Alcian blue staining.

2.4. MLO-Y4 culture and treatment

MLO-Y4 cells were cultured as previously reported[36]. The culture medium consisted of α-MEM, 10 % FBS (DearyTech, Uruguay, South America), 50 U/mL penicillin and 50 μg/mL streptomycin. MLO-Y4 cells at a density of 0.5×10^4 cells/well were plated in 24-well plates, treated with DMSO or C91 for 24 h, and then co-cultured with iMSCs at a density of 4×10^4 cells/well. For inhibition analysis, MLO-Y4 cells were treated with 10 μM C91 for 24 h, followed by treatment with iCRT-14 [40] at 1, 3, or 5 μM for another 24 h to measure the specificity of the role of Wnt signalling in MLO-Y4 on iMSCs differentiation.

2.5. Immunofluorescence analysis

Cells were cultured in the 24-well plates, fixed with 4 % paraformaldehyde for 15 min, and permeabilised in PBS containing 0.25 % Triton X-100 (PBS-T) for 30 min, both at room temperature. Then, the cells were blocked with 1 % BSA in PBS for 30 min. The primary and secondary antibodies used in this study are summarised in Table S1, and cells were incubated with each antibody for 1 h at room temperature. Nuclei were counterstained with DAPI (1:1000; Thermo Fisher Scientific; Norristown, PA, USA) for 5 min. Samples were observed and assessed using an inverted fluorescence microscope (Leica).

2.6. Western blot analysis

MLO-Y4 were treated with DMSO or 10 μM C91 for 24 h for β-catenin detection. The nuclear protein fraction of MLO-Y4 cells was obtained using a commercial nuclear protein extraction kit (Beyotime Biotechnology). In brief, cells were first suspended in cell lysis buffer containing PMSF, vortexed, and then centrifuged at 12,000×*g* and 4 °C for 5 min. The supernatant was carefully removed and a cell nuclear extraction buffer containing PMSF was added to the pellets. The pellets were vortexed and kept intermittently on ice for 30 min. Following this, the mixture was centrifugated at 12,000×*g* and 4 °C for 10 min, and the resulting supernatant was collected as the nuclear protein extract. Whole-cell lysates of DMSO control and COOME-treated iMSCs were lysed and sonicated in RIPA (Beyotime Biotechnology) lysis solution containing a phosphatase and protease inhibitor cocktail (Beyotime Biotechnology) for analysis of phosphorylation of SMAD1/5/8 and SMAD2/3. SDS-PAGE and blotting were performed using standard procedures. The PVDF membranes were blocked with 5 % BSA for 2 h at room temperature, followed by incubation overnight at 4 °C with specific primary antibodies, and 2 h at room temperature with secondary antibodies. Protein bands were detected using ECL Prime Western Blotting Detection Reagent (GE Healthcare, Little Chalfont, UK) and visualised using a Bio-Rad XRS chemiluminescence detection system (Bio-Rad, Hercules, CA, United states). The antibodies used in this study are listed in Supplementary Table S1.

2.7. RNA sequencing

Total RNA was extracted following the Trizol reagent protocol, with 3 μg of RNA used for each group's RNA sample preparation. Sequencing libraries were generated by purifying mRNA using poly T oligo-attached magnetic beads, followed by cDNA synthesis using random oligonucleotides and SuperScript II. Second-strand cDNA synthesis was performed using DNA Polymerase I and RNase H, with subsequent ligation of Illumina PE adapter oligonucleotides. The desired fragments (400–500 bp) were purified using the AMPure XP system and enriched via 15 PCR cycles using the Illumina PCR Primer Cocktail. After purification and quantification, sequencing was performed on a NovaSeq 6000 platform by Shanghai Personal Biotechnology Cp. Ltd. The fastp (version 0.22.0) was used to filter low-quality reads from the sequencing data or bioinformatics analysis. Differential gene expression analysis was performed using DESeq (version 1.38.3) with the criteria set at $|\log2FoldChange| > 1$ and a significant p-value <0.05. The Kyoto Encyclopedia of Genes and Genomes (KEGG) database was used to identify the relevant biological pathways associated with the clustered DEGs.

2.8. HUVECs tube formation assay

For the tube formation assay, HUVECs at a density of 1×10^5 cells/well, cell mixture of DMSO-MLO-Y4 (control) or COOME-treated iMSCs co-cultured with HUVECs at a 1:4 ratio was seeded onto 24-well plates pre-coated with 200 μL of Matrigel. The cells were then incubated for 6 h in a CO2 incubator at 37 °C following established procedures [41]. Subsequently, the capillary-like structures were observed and photographed under a microscope. The network of vascular tubes formed by HUVECs was quantified using the ImageJ software (64-bit, v1.46).

2.9. Neurogenesis and migration assay

MLO-Y4 cells treated with either DMSO or C91 for 24 h were plated at a density of 0.5×10^4 cells/well in a 24-well plate and co-cultured with iMSCs at a density of 4×10^4 cells/well. Simultaneously, 1×10^5 SH-SY5Y cells/well were added to the 6.5 mm Transwell with 8.0 μm Pore Polycarbonate Membrane Insert (pore size: 8.0 μm, Costar; Corning, NY, USA) placed onto each well of the 24-well plate. Cells were cultured for 48 h to allow for migration through the membrane. Migrated cells in the lower chambers of the transwells were stained with crystal violet staining solution, imaged, and quantified using ImageJ software. RNA from cells in 24-well plates and in the lower chambers of transwell plates was collected separately for subsequent analysis.

2.10. PCL and cell integrated 3D printing

3D printing was performed according to a previously reported previously [38]. Briefly, GelMA was fully dissolved in α-MEM to achieve a 20 % (w/v) concentration. 0.5 % (w/v) LAP was added to the GelMA solution, mixed thoroughly, and stored at 4 °C for future use. A mixture of 2×10^5 MLO-Y4 cells and 8×10^5 iMSCs was suspended in 0.5 mL of α-MEM. This cell suspension was subsequently combined with the GelMA solution and loaded in a syringe, which was cooled at 4 °C, preparing the contents for 3D printing.

Next, the polycaprolactone (PCL) particles were loaded onto a preheated hard-material nozzle. The molten PCL was extruded at 95 °C and a printing speed of 2 mm/s, with a strand diameter of 400 μm and an interval between strands of 1100 μm. Following this, the cell-loaded GelMA solution was printed between the PCL bands at a printing speed of 5 mm/s at a lowered temperature of 25 °C, with a beam diameter of 300 μm and an interval of 500 μm between beams. After printing one layer, 405 nm blue light was used to cross-link the hydrogel for 10 s. The process was then repeated vertically to print subsequent layers. Upon completion of the four layers, the PCL and cell-integrated 3D printing modules (PCI3D) were formed. The printed PCI3D modules were then placed in a cell growth medium in a 6-well plate and cultured at 37 °C with 5 % CO_2 for subsequent experiments.

2.11. Cell viability assay

The cell viability in the PCI3D modules was quantified using a live/dead viability assay kit. The cells were cultured for 1, 4, or 7 days, after which they were washed once with PBS and incubated in a staining mixture. This mixture was prepared by adding 1 μL of calcein AM (1000 ×) and 1 μL PI (1000 ×) to 1 mL of assay buffer. Calcein-AM stains live cells, while PI stains dead cells. The plates were then incubated in a 5 % CO_2 incubator at 37 °C for 30 min and immediately imaged with an

inverted fluorescence microscope (Leica, Wetzlar, Germany). Cell viability was quantified using ImageJ software (64-bit, v1.46).

2.13. Cell proliferative activity

The CCK-8 was used to evaluate the proliferative activity of cells in the PCI3D modules according to the manufacturer's instructions. Assessments were conducted on days 1, 4, and 7 after the start of culture. The PCI3D module was divided into six pieces, washed with PBS, and then placed in a 96-well plate, incubated in a 5 % CO_2 incubator at 37 °C for 2 h. Subsequently, the supernatant was transferred to a new 96-well plate, and the absorbance at 450 nm was measured using a Varioskan LUX multimode microplate reader (Thermo Fisher Scientific).

2.14. RNA extraction and qPCR analysis

Total RNA was extracted, and quantitative PCR (qPCR) was performed according to previously established protocols. Briefly, total RNA was extracted from cells using AG RNAex Pro Reagent (Accurate Biology, Changsha, China), and cDNA synthesis was performed using a reverse transcription reaction kit (Accurate Biology) in accordance with the manufacturer's instructions. Subsequently, qPCR was performed to quantify gene expression levels using the SYBR Green Premix Pro Taq HS qPCR Kit (Accurate Biology) with specific primer sets (listed in Tables S2 and S3) and analysed using the CFX96 Touch Real-Time PCR Detection System (Bio-Rad). Relative mRNA expression levels were normalised using the housekeeping genes glyceraldehyde-3-phosphate dehydrogenase of human origin (*GAPDH*) and the β-actin of mouse origin, applying the $2^{-\Delta\Delta Ct}$ method.

2.15. Alkaline phosphatase staining

AP staining was performed using a BCIP/NBT alkaline phosphatase colour-rendering kit. The cells were washed with PBS and fixed in 4 % formaldehyde for 5 min at room temperature. Subsequently, AP staining solution was applied to the cells and incubated for 30 min at room temperature. Importantly, the staining of the cells within the PCI3D module was conducted after 7 and 14 days, with the staining duration extended to 6 h. Staining results were recorded using a digital camera.

2.16. AP biochemical activity assay

The biochemical activity assay of AP was performed following established protocols [42]. After adding 50 mM Tris/HCl (pH 7.4) to the cells or PCI3D modules, cells were removed by scraping, followed by ultrasonic disruption for 30 s. The procedure was performed on ice. After centrifugation at 12,000×*g* for 3 min, the resulting supernatant was used in the alkaline phosphatase activity assay, following the manufacturer's instructions.

2.17. Mineralisation assay

The cells or PCI3D modules were initially cultured in growth medium for 3 days, after which bone nodule formation was induced in osteogenic medium containing 0.1 mM dexamethasone, 10 mM β-glycerophosphate disodium salt solution, and 50 μg/mL L-ascorbic acid for 14 or 28 days. The mineralised modules were stained using the alizarin red S Staining Kit (Beyotime Biotechnology) following the manufacturer's instructions and subsequently photographed under a microscope. Following this, the stained mineralised modules were thoroughly washed with PBS and then subjected to destaining in 10 % cetylpyridinium chloride for 1 h. The absorbance of the destained solution was measured at 562 nm to quantify mineralisation status.

2.18. Statistical analysis

Statistical analyses were performed using GraphPad Prism 9.5.1 software. Each experiment was independently repeated three times. Data are presented as mean ± SD. The normal distribution of the data was confirmed using normality tests. One-way ANOVA was used to analyse the differences among multiple groups. An independent or paired *t*-test was performed between two comparable groups, depending on the data structure. A *p*-value of less significance was set at $p < 0.05$.

3. Results

3.1. Stable directed differentiation of iMSCs from hiPSCs

We used a highly effective method previously established [39] with minor modifications to induce MSCs from hiPSCs. We used a ready-to-use coating solution, PSCeasy, and a chemically defined, animal-origin-free PGM1 medium for iPSC expansion and iNCC induction. This streamlined procedure simplifies the operations and reduces costs (Fig. 1A). The induction of NCCs was initiated by replacing the PGM1 with an NCC induction medium, which constituted CDM supplemented with TGF-β and GSK-3β signalling inhibitors. Cells were harvested 10–12 days after differentiation, subjected to flow cytometric analysis (FACS), and sorted using the NCC marker CD271. At this stage, the induction rate of $CD271^+$ iNCCs was approximately 83 % (Fig. 1B). The iNCCs were cultured in maintenance medium (CDM supplemented with SB431542, EGF and bFGF) for 5–7 passages, after which MSC induction was performed by replacing the medium with αMEM containing 10 % FBS and bFGF.

The iNCCs exhibited a spindle-like morphology, whereas the iMSCs displayed an elongated, fibroblastic, and MSC-like morphology (Fig. 1C). Additionally, they demonstrated a decreased expression of pluripotency genes (*ZFP42* and *SOX2*) (Fig. 1D) and increased expression profiles consistent with NCCs (*NGFR* and *TFAP2A*) (Fig. 1E) and MSCs (*CD13*, *CD44*, *CD73*, *CD90* and *CD105*) (Fig. 1F). The expression of MSC marker genes in iMSCs gradually increased from passages 1 and 2 and then stabilised from passages 3 to 5, indicating that differentiation reached a plateau after the third passage. As CD90 is also robustly expressed in iPSCs [43–45], iMSCs exhibited lower CD90 expression at passage 1 and passage 2, and no significant difference from passages 3 to 5 compared to iPSCs.

We performed immunostaining for E-cadherin and Vimentin, which are specific markers for iPSCs [46,47] and mesenchymal cells [48], respectively. iMSCs were negative for E-cadherin expression and positive for Vimentin expression, indicating successful differentiation from iPSCs (Fig. 1G). Immunostaining revealed that the expression of pluripotency markers OCT4, NANOG, and SOX2 were negative in iMSCs, indicating the absence of undifferentiated cells (Fig. 1H). The iMSCs demonstrated typical trilineage differentiation into cartilage, bone, and adipose lineages under the respective induction conditions (Fig. 1I). The proliferation status of each generation of iMSCs from day 3 (passages 1) to day 15 (passage 5) remained stable (Fig. 1J). These results suggest that the MSCs induction method used in this study effectively directed their fate towards the mesenchymal lineage, resulting in a stable and expandable iMSCs population.

3.2. Effects of C91-Induced osteocytes on osteoblast differentiation and mineralisation of iMSCs

Our previous studies have confirmed that C91-treated osteocytes can significantly activate osteogenic differentiation in ST2 cells [37]. Graded concentrations (0, 1, 5, 10, and 15 μM) of C91 were evaluated to determine the optimal osteogenic microenvironment for iMSC differentiation formed by C91-treated murine osteocyte-like cell line (MLO-Y4). MLO-Y4 cells were treated with C91 for 24 h, after which the drug was withdrawn and the cells were co-cultured with iMSCs for 3 or

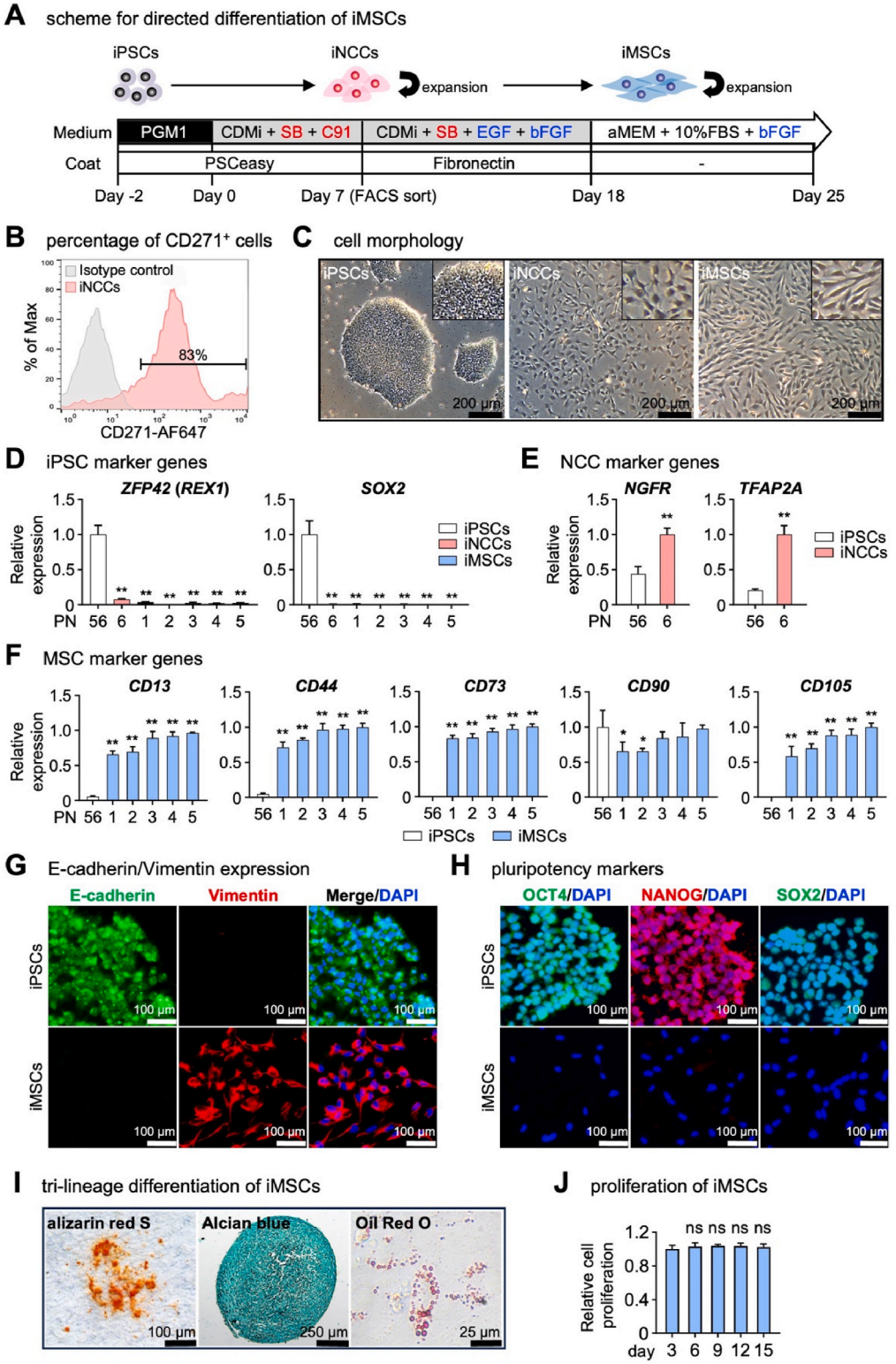

Fig. 1. Induction and characterisation of iMSCs from iPSCs. (A) Schematic representation of mesenchymal stem cells induction protocol. **(B)** Flow cytometry sorting of CD271-positive neural crest. **(C)** Cell morphology at different induction stages. The induction of chondrogenic, osteogenic, and adipogenic lineages was evaluated using Alcian blue, Oil Red O and alizarin red S staining, respectively. **(D)** The expression of iPSC marker genes in iPSC (passage 56), iNCC (passage 6) and iMSC (from passage 1 to passage 5) was detected using qPCR. **(E)** qPCR analysis of the expression of NCC marker genes. **(F)** qPCR assay for the expression of MSC marker genes. The expression levels of all genes were normalised to the internal reference in the same group. All data are presented as mean ± SD, $n = 3$. $^{*}p < 0.05$; $^{**}p < 0.01$ using one-way ANOVA **(D** and **F)** and *t*-test **(E)** versus iPSC group. **(G)** Immunostaining results for E-cadherin and Vimentin. **(H)** Immunofluorescence analysis shows negative OCT4, NANOG and SOX2 protein expression in iMSCs. **(I)** Tri-lineage differentiation properties of iMSCs. **(J)** Proliferation status of iMSCs during expansion culture. The graph illustrating the relative cell proliferation ratio of iMSCs from day 3 (passages 1) to day 15 (passage 5). All data are presented as mean ± SD, $n = 3$. n.s., no significant difference using one-way ANOVA versus day 3 group. (For interpretation of the references to color in this figure legend, the reader is referred to the Web version of this article.)

21 days for further analysis (Fig. 2A). Alkaline phosphatase (AP) staining (Fig. 2B) and a biochemical activity assay (Fig. 2C) showed that the 5, 10 and 15 μM C91-treated group exhibited significantly elevated osteogenic differentiation compared to that of the DMSO-treated control group. The expression of human osteoblast marker genes *ALPL*, *RUNX2*, *BGLAP* and *COL1α*, as detected using qPCR, exhibited a stable increase with 10 μM of C91 (Fig. 2D). Consequently, we used 10 μM C91-treated MLO-Y4 in the study to establish the osteogenic microenvironment (COOME), unless otherwise specified. Mineralisation induction experiments revealed that the C91-treated group formed larger and denser mineral nodules than the DMSO control group, as indicated using alizarin red S staining (Fig. 2E and F). These results indicated that COOME facilitates the differentiation of iMSCs into osteoblasts.

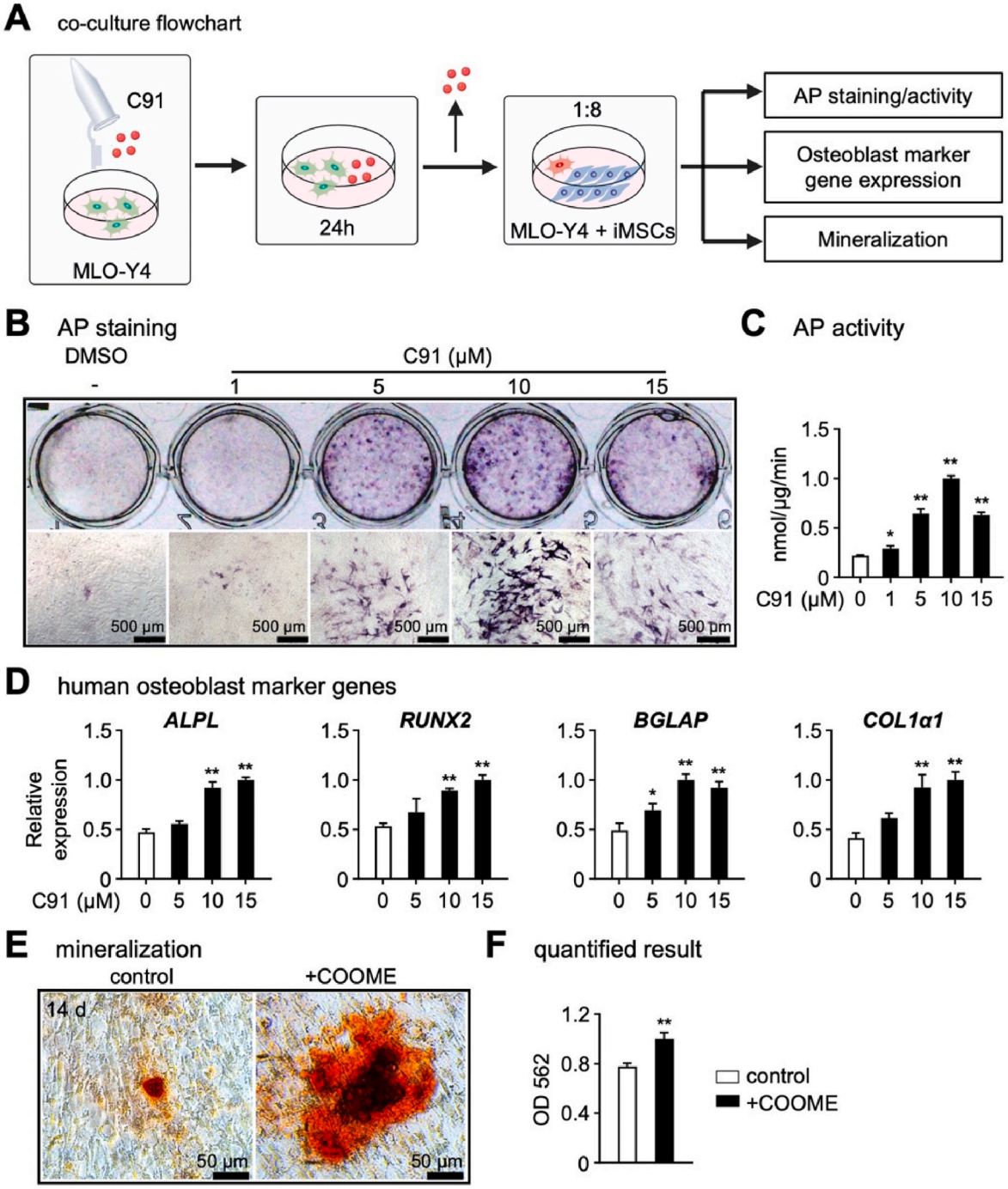

Fig. 2. Effects of C91-treated osteocytes on osteogenic differentiation in iMSCs. (A) Co-culture flowchart. MLO-Y4 cells were treated with 1, 5, 10, or 15 μM of C91 for 24 h. Subsequently, these cells were co-cultured with iMSCs for the following experiments. **(B)** Osteogenic differentiation was assessed using AP staining. iMSCs co-culturing with DMSO-treated MLO-Y4 cells were used as the control group. The lower images are enlargements of the upper images; scale bars: 500 μm. **(C)** Quantification analysis of AP biochemical activity. **(D)** qPCR analysis of the expression of osteoblast marker genes. All data are presented as mean ± SD, $n = 3$. *$p < 0.05$; **$p < 0.01$ using one-way ANOVA versus DMSO control. **(E** and **F)** iMSCs were co-cultured with COOME in growth medium for 3 days and in osteogenic medium for another 21 days for mineralisation assay. The mineralised bone nodules were photographed after alizarin red S staining (**E**), followed by quantification assay **(F)**. Scale bars: 500 μm. All data are presented as mean ± SD, $n = 3$. **$p < 0.01$ versus DMSO control using the *t*-test. (For interpretation of the references to color in this figure legend, the reader is referred to the Web version of this article.)

3.3. C91 activates the Wnt/β-catenin signalling pathway in MLO-Y4 and affects iMSCs

A critical event in the canonical Wnt/β-catenin signalling pathway is the translocation of β-catenin from the cytoplasm to the nucleus. We conducted immunofluorescence assays to examine intracellular β-catenin distribution in MLO-Y4 cells to assess whether C91 activates Wnt signalling via this pathway. Following C91 treatment, a pronounced co-localisation of GFP-labelled β-catenin with DAPI-stained nuclei was observed, significantly more intense than that in the DMSO control (Fig. 3A). Western blot analysis also revealed that C91 treatment resulted in an increase in nuclear β-catenin levels, indicating C91 facilitates β-catenin's translocation into the nucleus (Fig. 3B). Additionally, qPCR assays confirmed the upregulation of Wnt target genes, such as *Lef1, Axin2*, *Cxcl43*, and *Ccnd4* (Fig. 3C), indicating that C91 activates the canonical Wnt/β-catenin signalling pathway in MLO-Y4 cells.

The interaction between Wnt signalling and fibroblast growth factor 2 (FGF2) is critical in regulating osteoblastic differentiation [49,50]. FGF2 interacts with BMP and TGF-β signalling by repressing phosphorylation of SMAD1/5/8 (pSMAD1/5/8) or promoting pSMAD2/3, allowing for the maintenance of cells in the undifferentiated state [51], thereby inhibiting MSCs' osteogenic differentiation [52,53]. Furthermore, Wnt/β-catenin signalling in osteocytes regulate the production of BMP and TGF-β ligands [54,55]. The qPCR results showed a decreased expression of *Fgf2* after C91 treatment (Fig. 3C). Meanwhile, western blotting assays revealed enhanced pSMAD1/5/8 (Fig. 3D), cytoplasmic transducers of BMP signalling, and reduced pSMAD2/3 (Fig. 3E), cytoplasmic transducers of TGF-β signalling, in COOME-treated iMSCs. These findings suggest the involvement of canonical Wnt signalling in COOME-mediated osteogenic differentiation of iMSCs.

3.4. Specificity of Wnt/β-catenin signalling in COOME on iMSCs osteogenic differentiation

We used the inhibitor of β-catenin-responsive transcription 14 (iCRT14) to determine the essential role of canonical Wnt signalling in C91-activated osteocytes for iMSC osteogenic differentiation. This inhibitor disrupts the interaction between β-catenin and T cell factor/lymphoid enhancer factor (TCF/LEF) transcription complexes [40]. qPCR results revealed that 5 μM iCRT14 effectively downregulated the expression of Wnt target genes *Lef1* and *Axin2*, which had been upregulated by C91 (Fig. 4A). AP staining and activity assay results demonstrated that iCRT14 counteracted the osteogenic effects previously enhanced by COOME by inhibiting osteogenic activity in iMSCs (Fig. 4B and C). Additionally, iCRT14 suppressed the elevated expression of human osteoblast marker genes *RUNX2*, *ALPL* and *OSX* induced by COOME (Fig. 4D). These findings collectively emphasise the critical role of the Wnt/β-catenin signalling pathway within COOME in promoting osteogenic differentiation in iMSCs.

3.5. Gene expression profiles of COOME-treated iMSCs

We conducted a global transcriptome analysis to gain deeper insights into the marker gene expression of iMSCs treated with COOME compared to that of the DMSO control group. Correlation analysis of gene expression levels across different samples confirmed biological reproducibility (Fig. 5A). We identified 259 genes in the COOME-treated group that exhibited differential expression compared to the control group, with 139 upregulated and 120 downregulated (Fig. 5B).

KEGG pathway analysis revealed the top 20 upregulated pathways in COOME-treated iMSCs (Fig. 5C). The upregulated genes were enriched in pathways associated with growth hormone production, axon guidance, chemokine signalling, cellular senescence, and cytoskeleton regulation. These results indicate that COOME treatment enhances the biological activity of iMSCs to influence the surrounding environment by regulating biological processes such as vasculature and neural generation. This supported the potential of COOME-iMSCs to integrate into the tissue environment and regulate post-transplantation bone tissue regeneration.

Heatmaps indicated that representative genes related to bone formation were upregulated in COOME-treated iMSCs (Fig. 5D), supporting the hypothesis that COOME promotes the osteogenic differentiation and mineralisation of iMSCs. Furthermore, genes related to proangiogenesis (Fig. 5E) and proneurogenesis (Fig. 5F) were upregulated in iMSCs following COOME treatment. Collectively, these findings suggested that COOME may create a microenvironment that enhances the differentiation of iMSCs into osteoblasts while promoting their biological activities.

3.6. Effects of COOME-treated iMSCs on angiogenesis and neurogenesis

We assessed angiogenic responses following co-culturing with human umbilical vein endothelial cells (HUVECs) to examine the potential of the COOME co-culture system with iMSCs to induce angiogenesis. We observed a significant increase in the expression of the angiotrophic factor genes *VEGF* and *PDGF* in COOME-treated iMSCs (Fig. 6A) and the vascular marker genes *VEGFR2* and *PDGFRB* in the HUVEC-COOME-iMSC co-culture group (Fig. 6B) compared to that of the DMSO control group. Additionally, enhanced vascular tubule formation (Fig. 6C) and an increased number of tubular nodes, total length, and number of branches (Fig. 6D) were observed in the HUVEC-COOME-iMSC co-culture group.

We investigated the neurogenic effects of COOME-treated iMSCs on SH-SY5Y cells, a well-established human neuroblastoma cell line that is used to study neuronal differentiation. The expression of neurotrophic factor genes *FGF2* and *GDNF* was increased in COOME-treated iMSCs (Fig. 6E), along with the upregulation of neuro-marker genes NTN1 and PAX6 in the SH-SY5Y-COOME-iMSC co-culture group (Fig. 6F). COOME-treated iMSCs showed significantly enhanced migration of SH-SY5Y cells (Fig. 6G and H). These results suggested that COOME-treated iMSCs exhibit enhanced angiogenic and neurogenic potential, which are crucial for osteogenesis *in vivo* and contribute to an improved microenvironment for bone formation and regeneration.

3.7. Construction of iMSC-Containing PCI3D modules with enhanced osteogenic capability

We established a PCL and cell-integrated 3D printing (PCI3D) system [38]. This system utilises the alternating printing of PCL bundles from a heating cartridge and GelMA hydrogel bundles loaded with cells. This resulted in a stable support structure with appropriately sized connecting channels, which facilitated the efficient transport of nutrients and metabolites (Fig. 7A). This approach enables the creation of biofabricated functional 3D modules that faithfully replicate the *in vivo* osteogenic processes and provide valuable bone graft materials for tissue engineering. We used this system to construct a 3D module containing COOME and iMSCs with enhanced osteogenic functionality in the present study. PCI3D modules containing cells were cultured for 1, 4, or 7 days to assess cell viability. Live/dead cell assays were performed using Calcein AM and PI staining (Fig. 7B and C). The results indicated a high cell viability rate (99.5 %) in both the experimental and control groups, confirming that PCI3D functional modules created a conducive environment for cell survival. Additionally, a proliferative activity assay using CCK-8 revealed comparable linear increases in cell numbers between the groups (Fig. 7D). These findings suggested that the PCI3D module provides a favourable environment for the growth and proliferation of iMSCs.

Subsequently, the PCI3D modules containing COOME-iMSCs were subjected to osteoblast differentiation assays. AP staining and biochemical activity assays revealed a significant enhancement in osteogenic differentiation within the PCI3D modules with COOME compared to the DMSO control modules (Fig. 8A and B). This was further confirmed through qPCR analysis, with the COOME group

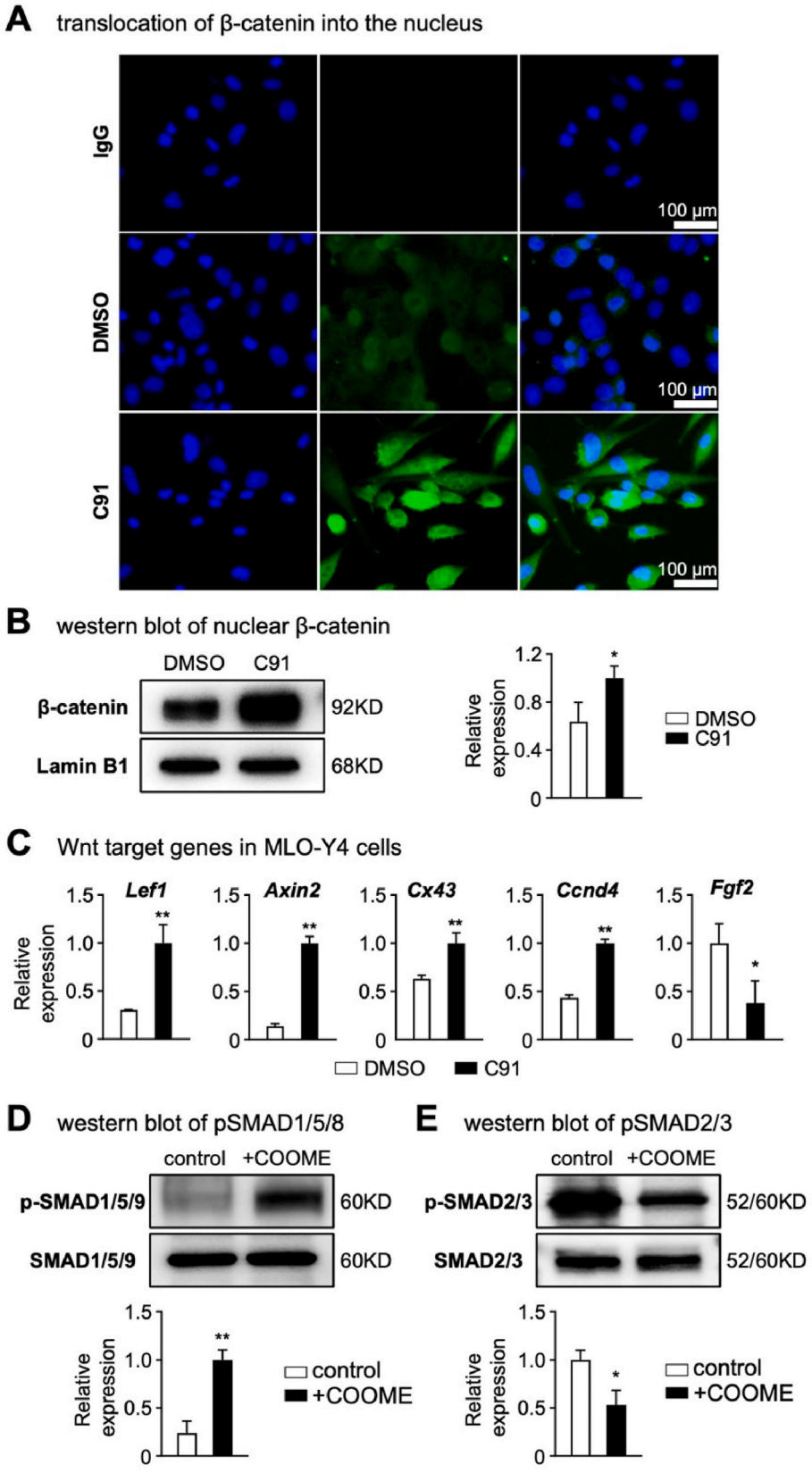

Fig. 3. Effects of C91 on the canonical Wnt signalling pathway in MLO-Y4 cells. (**A**) Immunofluorescence detected β-catenin in MLO-Y4 cells treated with DMSO or 10 μM C91. DAPI was used to stain the nucleus. **(B)** Western blot detection of protein β-catenin expression in the nucleus of MLO-Y4 cells. Lamin B1 (nucleus) was used as the internal control. Representative image (left) and quantification result (right) are shown. **(C)** Increased expression of Wnt target genes detected using qPCR in MLO-Y4 cells treated with DMSO or C91 for 24 h. **(D** and **E)** Western blotting assay of pSMAD1/5/8 **(D)** and pSMAD2/3 **(E)** in iMSCs treated with DMSO control or COOME. Quantification of relative SMAD1/5/8 or SMAD2/3 phosphorylation levels normalised to total SMAD1/5/8 or SMAD2/3. All data are presented as mean ± SD, $n = 3$. $^{*}p < 0.05$; $^{**}p < 0.01$ using the *t*-test versus DMSO **(B** and **C)**, or control **(D** and **E)** group.

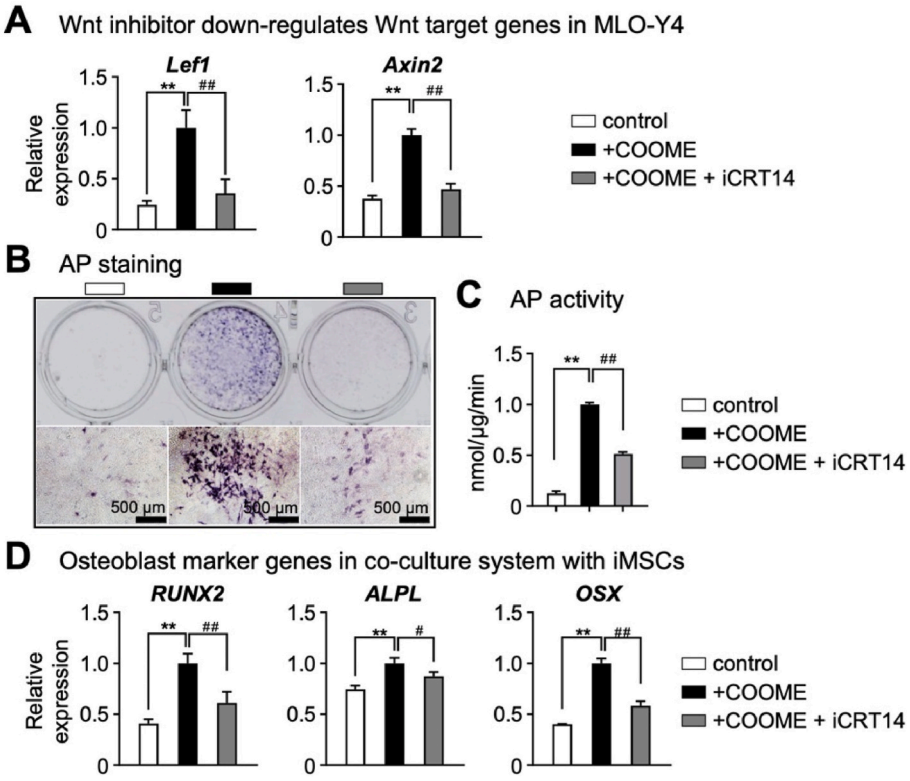

Fig. 4. Effects of inhibition of Wnt/β-catenin signalling in the COOME on osteogenic differentiation of iMSCs. (A) The expression of Wnt target genes in MLO-Y4 cells was detected using qPCR. **(B)** The COOME was treated with or without Wnt inhibitor ICRT 14 (1, 3 or 5 μM) for 24 h. Then the treated COOME was co-culture with iMSCs for 3 days. Osteogenic differentiation was evaluated using AP staining. **(C)** Quantification analysis of AP biochemical activity. **(D)** qPCR analysis of the expression of osteoblast marker genes in a co-culture system. All data are presented as mean ± SD, $n = 3$. $^{*}p < 0.05$; $^{**}p < 0.01$ versus DMSO group using one-way ANOVA; $\#p < 0.05$; $\#\#p < 0.01$ versus COOME group using one-way ANOVA.

exhibiting a significant increase in the expression of osteoblast markers genes, including ALPL, COL1α1, and BSP, in comparison to that of the DMSO control group (Fig. 8C). PCI3D modules were initially cultured in full growth medium for 3 days, followed by 21 days in osteogenic medium to assess the impact of COOME on bone mineralised nodule formation. Alizarin red S staining and quantitative analysis revealed that the COOME module exhibited an increased number of calcium nodules (Fig. 8D), confirming COOME's promotion of iMSC mineralisation by COOME. Therefore, COOME-treated iMSCs in 3D bioprinted modules demonstrated their capability as functional biomaterials for the formation of authentic bone.

4. Discussion

Recent advances in transplant materials and 3D-printing have significantly improved the tissue compatibility and shape adaptability of artificial bone grafts, primarily focusing on addressing the insufficient biological activity in synthetic implants [56,57]. The incorporation of seed cells imparts synthetic implants for active tissue generation [58]. In this study, we generated homogeneous iMSCs as ideal seed cells using a stable directed differentiation system. In addition, COOME, a microenvironment derived from osteocytes, effectively enhanced osteogenic differentiation (ALP staining, activity, and osteogenic marker gene expression) and mineralisation of iMSCs by activating the canonical Wnt signalling pathway and upregulated the pro-angiogenesis and pro-neurogenesis capacity of iMSCs. The superior osteogenic differentiation and mineralisation abilities of COOME-iMSCs were confirmed in a Bio3D module mimicking an *in vivo* environment. These results underscore the potential of COOME-iMSCs to address the biological challenges associated with artificial bone transplantation.

Currently, a major industrial challenge in the clinical application of iMSCs is the lack of a well-defined culture system for homogeneous iPSC-iMSC production [8,59]. Among the mainstream methods for iMSC generation, embryoid body generation is a complex and time-consuming process. Diverse differentiation pathways within the embryoid body result in the distinct phenotypes and functions of target cells [60–64]. In contrast, the one-step induction method is straightforward and directly applies specific factors to iPSCs to drive their differentiation towards iMSCs [17–19,65,66]. However, inconsistencies in cellular responses persist during induction. Additionally, the cellular properties may undergo unstable changes during induction and subsequent passages, contributing to iMSCs heterogeneity. Moreover, current iMSC induction methods often lack specific steps for sorting the target cells, resulting in a final product containing diverse cellular subpopulations. Our two-step method induced iMSCs through the NCC lineage, mimicking embryonic development, to address these challenges. This protocol exclusively utilises a chemically defined, animal-origin-free medium containing minimal chemical signalling inhibitors and growth factors and uses FACS sorting to purify iNCCs. Thus, we successfully generated a robust, homogeneous, and functionally stable iMSC population. This approach improves the feasibility and reliability of iMSCs and paves the way for their scalable production and utilisation in clinical applications.

Another significant challenge for the clinical application of iMSCs in bone regeneration and repair is their insufficient osteogenic capacity [23–26]. Current efforts to enhance the osteogenic capability of MSC-containing materials or incorporate growth factors face limitations owing to sustained osteogenesis and potential side effects [27–31]. The osteogenic microenvironment has been reported to guide the directed differentiation of seed cells, creating a conducive niche for cell growth and enhancing osteogenesis post-transplantation [67]. Osteocytes, as primary regulators of the bone microenvironment through both endocrine and paracrine signalling, influence cells that are relevant to bone

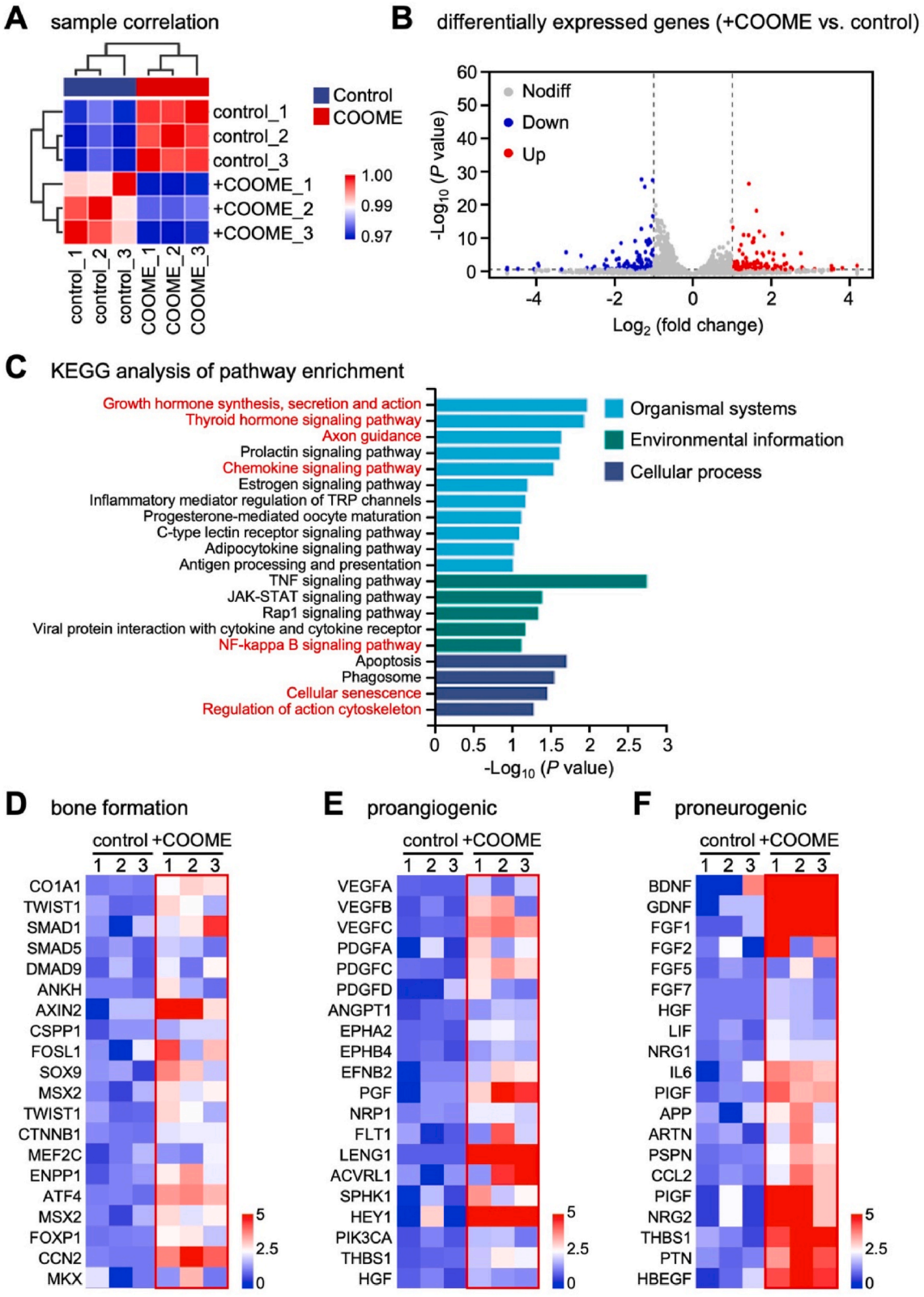

Fig. 5. RNA-sequencing assessment of the effects of COOME on iMSCs. (A) Sample correlation in gene expression patterns. **(B)** Volcano plot illustrating differentially expressed genes in iMSCs treated with either DMSO control or COOME. **(C)** KEGG analysis identifying the top 20 regulated pathways in the COOME group, compared to the DMSO control group. **(D-F)** Heatmaps displaying the expression of representative genes related to bone formation **(D)**, pro-adipogenesis **(E)** and pro-neurogenesis **(F)** in iMSCs from DMSO control and COOME groups.

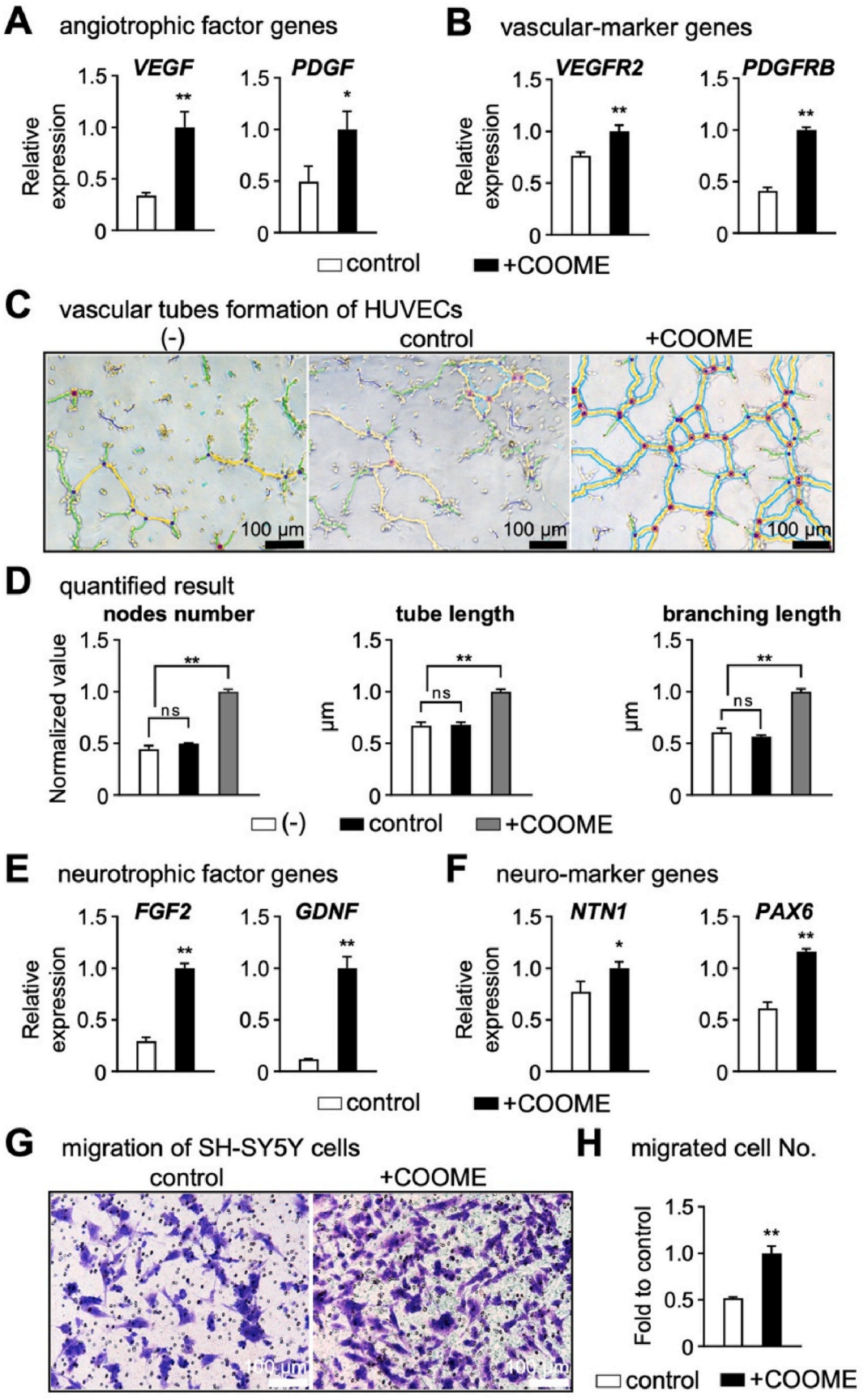

(caption on next page)

Fig. 6. Modulation of angiogenesis and neurogenesis by COOME-treated iMSCs. A-D. Potential of the COOME-treated iMSCs to induce angiogenesis. **A.** qPCR analysis of the expression of angiotrophic factor genes in control and COOME-treated iMSCs. B. qPCR for vascular-marker genes in HUVECs co-cultured with control and COOME-treated iMSCs. **C.** Images of vascular tubules formation assay. **D.** Quantification of nodes number, tube length and branching length of formed nodes. **E-H.** Potential of the COOME-treated iMSCs to induce neurogenesis. **E.** qPCR analysis of the expression of neurotrophic factor genes in control and COOME-treated iMSCs. **F.** qPCR for neuro-marker genes in SH-SY5Y co-cultured with control and COOME-treated iMSCs. **G.** Images of SH-SY5Y migration assay. **H.** Quantification of migrated cell number. All data are presented as mean ± SD, $n = 3$. $^{*}p < 0.05$; $^{**}p < 0.01$ versus the control group using the *t*-test **(A, B, E, F** and **H)**, or versus (−) (HUVECs only) group using one-way ANOVA **(D)**.

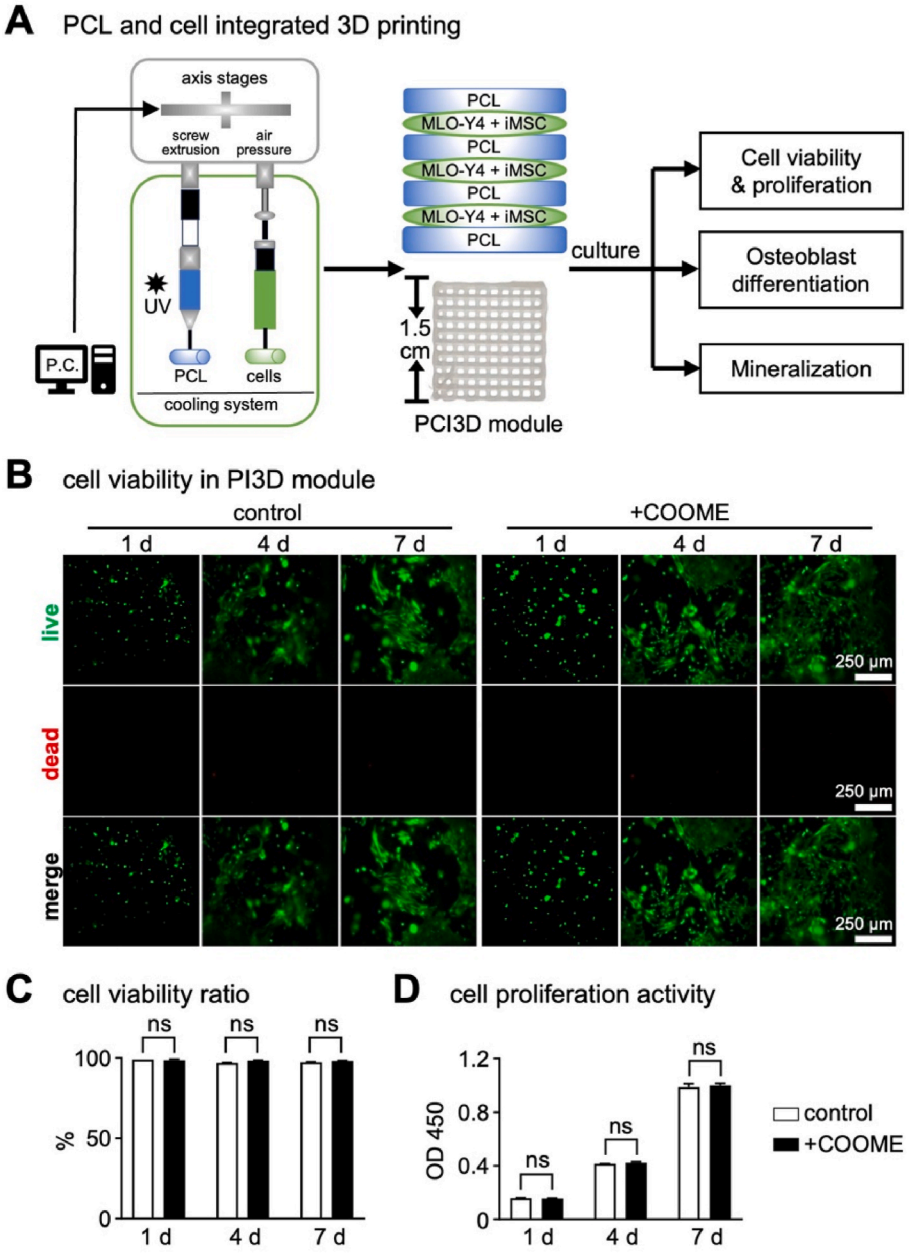

Fig. 7. Effects of the COOME in PCI3D modules on cell survival and growth. (A) Schematic representation of the PCL and cell-integrated 3D printer (left), the printed module with PCL beams and cell-laden hydrogel beams (center), and overview of the subsequent experimental design (right).**(B and C)** Live/dead cell assay was performed to assess cell survival and proliferation at specific time points (1, 4, and 7 days of *in vitro* culture). Live cells were stained with calcein-AM (green), while dead cells were identified as EthD-1 negative (red). Scale bars: 250 μm. Representative image **(B)** and quantification results **(C)** are presented. **(D)** Proliferation activity was evaluated using imaging and a CCK-8 assay kit. All data are presented as mean ± SD, n = 3. n.s., no significant difference using the *t*-test versus the DMSO group. (For interpretation of the references to color in this figure legend, the reader is referred to the Web version of this article.)

regeneration [54,68,69]. Our study innovatively created a cell-microenvironment composite with superior osteogenic capacity by combining iMSCs with a safe and effective microenvironment provided by C91-activated osteocytes. COOME establishes a microenvironment that promotes appropriate osteogenic differentiation of iMSCs, laying the foundation for the large-scale production of precisely regulated bone grafts.

Our results indicate that COOME treatment enhances the biological

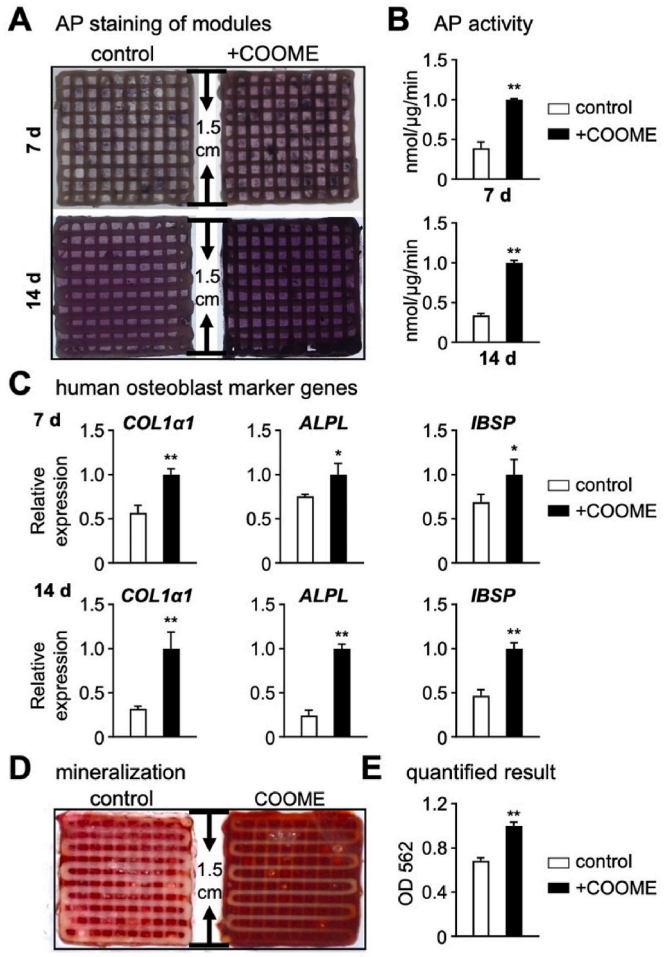

Fig. 8. Effects of COOME on osteoblast differentiation and mineralisation of iMSCs in PCI3D modules. **(A)** AP staining and **(B)** AP activity assay of iMSCs in PCI3D modules (7 and 14 days of *in vitro* culture). **(C)** qPCR analysis of the expression of human osteoblast marker genes in PCI3D modules. **(D and E)** Cell-integrated PCI3D modules cultured in growth medium for 3 days and in osteogenic medium for another 21 days for mineralisation assay. The mineralised bone nodules were photographed after alizarin red S staining **(D)**, followed by quantification assay **(E)**. All data are presented as mean ± SD, $n = 3$. $^{*}p < 0.05$; $^{**}p < 0.01$ versus the control group using the *t*-test. (For interpretation of the references to color in this figure legend, the reader is referred to the Web version of this article.)

activity of iMSCs. The successful integration of bone grafts and the regeneration of bone tissue rely crucially on their vascularisation and neuralisation activities, which provide nutrients and oxygen, remove waste, and perceive environmental changes, thereby facilitating bone healing [70–72]. Current strategies to achieve vascular/neuro-bone tissue engineering involve scaffold materials incorporating endothelial cells/Schwann cells or acellular active factors [73–76], which face challenges in effectiveness and side effects. *In vivo* and *in vitro* evidence suggests that MSCs can support both angiogenesis and neurogenesis [20,77]. Our study provides valuable insights into COOME-iMSCs in environments conducive to vascular and neural bone tissue engineering.

In this study, we used 3D bioprinted models to simulate the *in vivo* microenvironment to the greatest extent. The 3D bioprinted tumor organoid models can be used for personalised drug screening and precise treatment of patients, thereby predicting the sensitivity, specificity, and accuracy of chemotherapy regimens [78,79]. Cells within 3D models offer advantages in establishing proper cell functions and associated signalling pathways, enhancing the accuracy of evaluating therapeutic effects in a physiologically relevant context [80]. This indicates that the 3D module can be used to predict the bone regeneration effect of COOME-iMSCs *in vivo*. Further development of microenvironment-modulated 3D-printed bone grafts will provide more extensive possibilities for clinical applications such as bioactive implants. In addition, we combined human-derived iMSCs with the osteogenic microenvironment generated by the murine cell line MLO-Y4 to create a cell-microenvironment composite with superior osteogenic capability. By analysing the expression of human target genes, we clarified the positive impact of COOME on iMSCs in terms of osteogenesis, angiogenesis, and neurogenesis. Additionally, by evaluating the activation and targeted inhibition of the classical Wnt signalling pathway in MLO-Y4 cells, we validated the mechanism by which COOME exerts its effects. This comprehensive research design provides profound insights into the regulation of iMSC functionality by COOME, demonstrating its efficacy across species. However, whether this effect is a result of direct cell-cell interactions or indirect pathways involving protein secretion remains unclear and requires further exploration. Furthermore, gradual improvements in the sources of COOME (such as porcine or bovine origin) and preparation methods (such as decellularised matrices, bioinks, and exosomes) are essential for its optimal application in clinical practice.

5. Conclusion

In summary, we successfully generated iMSCs with highly osteogenic, pro-angiogenic, and neurogenic capabilities using COOME, which is based on activating canonical Wnt signalling in osteocytes. Combining COOME-iMSCs with a 3D bioprinting system for tissue engineering is a promising avenue for creating shape-matched and functional bioactive bone implants. It offers a promising strategy for addressing the clinical application of bone defects and advancing regenerative medicine.

Funding

This work was supported by the Young Scientists Fund of the National Natural Science Foundation of China (Grant No. 82202655) to C. Z., National Natural Science Foundation of China (U1601220, 82072450), Chongqing Natural Science Foundation Innovation and Development Joint Fund (CSTB2022NSCQ-LZX0048) to X.T., and CQMU Program for Youth Innovation in Future Medicine (W0144) to M. Z.

CRediT authorship contribution statement

Qiuling Guo: Writing – original draft, Visualization, Validation, Methodology, Investigation, Formal analysis, Data curation. **Jingjing Chen:** Methodology, Investigation, Data curation. **Qiqi Bu:** Methodology, Investigation, Data curation. **Jinling Zhang:** Visualization, Methodology, Investigation, Data curation. **Minjie Ruan:** Visualization, Project administration, Methodology, Formal analysis, Data curation. **Xiaoyu Chen:** Data curation, Investigation, Methodology. **Mingming Zhao:** Methodology, Resources, Supervision, Writing – review & editing. **Xiaolin Tu:** Writing – review & editing, Supervision, Resources, Funding acquisition, Conceptualization. **Chengzhu Zhao:** Writing – review & editing, Writing – original draft, Supervision, Resources, Project administration, Funding acquisition, Conceptualization.

Declaration of competing interest

The authors declare that they have no known competing financial interests or personal relationships that could have appeared to influence the work reported in this paper.

Data availability

Data will be made available on request.

Acknowledgments

We thank M. Ikeya (Center for iPS Cell Research and Application, Kyoto University, Kyoto, Japan) for advices on iMSC and tri-lineage induction experiments; A. Jin for providing experimental facilities and conditions, X. Han and C. Hu for technical assistance on FACS experiments (Chongqing Key Laboratory of Basic and Translational Research of Tumor Immunology, Chongqing Medical University, Chongqing, China); and members of the X.T. laboratory for their support throughout this study.

Appendix A. Supplementary data

Supplementary data to this article can be found online at https://doi.org/10.1016/j.mtbio.2024.101111.

References

[1] A. Stahl, Y.P. Yang, Regenerative approaches for the treatment of large bone defects, Tissue Eng., Part B 27 (6) (2021) 539–547.
[2] P. Dec, A. Modrzejewski, A. Pawlik, Existing and novel biomaterials for bone tissue engineering, Int. J. Mol. Sci. 24 (1) (2022).
[3] O. Omar, T. Engstrand, L. Kihlström Burenstam Linder, J. Åberg, F.A. Shah, A. Palmquist, U. Birgersson, I. Elgali, M. Pujari-Palmer, H. Engqvist, P. Thomsen, In situ bone regeneration of large cranial defects using synthetic ceramic implants with a tailored composition and design, Proc. Natl. Acad. Sci. U. S. A. 117 (43) (2020) 26660–26671.
[4] E.C. Rodríguez-Merchán, Bone healing materials in the treatment of recalcitrant nonunions and bone defects, Int. J. Mol. Sci. 23 (6) (2022).
[5] H. Lin, J. Sohn, H. Shen, M.T. Langhans, R.S. Tuan, Bone marrow mesenchymal stem cells: aging and tissue engineering applications to enhance bone healing, Biomaterials 203 (2019) 96–110.
[6] Y. Qin, J. Guan, C. Zhang, Mesenchymal stem cells: mechanisms and role in bone regeneration, Postgrad. Med. 90 (1069) (2014) 643–647.
[7] Z. Poon, W.C. Lee, G. Guan, L.M. Nyan, C.T. Lim, J. Han, K.J. Van Vliet, Bone marrow regeneration promoted by biophysically sorted osteoprogenitor from mesenchymal stromal cells, Stem Cells Transl Med 4 (1) (2015) 56–65.
[8] C. Zhao, M. Ikeya, Generation and applications of induced pluripotent stem cell-derived mesenchymal stem cells, Stem Cell. Int. 2018 (2018) 9601623.
[9] D. Sheyn, S. Ben-David, G. Shapiro, S. De Mel, M. Bez, L. Ornelas, A. Sahabian, D. Sareen, X. Da, G. Pelled, W. Tawackoli, Z. Liu, D. Gazit, Z. Gazit, Human induced pluripotent stem cells differentiate into functional mesenchymal stem cells and repair bone defects, Stem Cells Transl Med 5 (11) (2016) 1447–1460.
[10] Q. Wu, B. Yang, K. Hu, C. Cao, Y. Man, P. Wang, Deriving osteogenic cells from induced pluripotent stem cells for bone tissue engineering, Tissue Eng., Part B 23 (1) (2017) 1–8.
[11] Y. Jung, G. Bauer, J.A. Nolta, Concise review: induced pluripotent stem cell-derived mesenchymal stem cells: progress toward safe clinical products, Stem Cell. 30 (1) (2012) 42–47.
[12] O. Bar-Nur, H.A. Russ, S. Efrat, N. Benvenisty, Epigenetic memory and preferential lineage-specific differentiation in induced pluripotent stem cells derived from human pancreatic islet beta cells, Cell Stem Cell 9 (1) (2011) 17–23.
[13] Y. Tan, S. Ooi, L. Wang, Immunogenicity and tumorigenicity of pluripotent stem cells and their derivatives: genetic and epigenetic perspectives, Curr. Stem Cell Res. Ther. 9 (1) (2014) 63–72.
[14] D. Doi, H. Magotani, T. Kikuchi, M. Ikeda, S. Hiramatsu, K. Yoshida, N. Amano, M. Nomura, M. Umekage, A. Morizane, J. Takahashi, Pre-clinical study of induced pluripotent stem cell-derived dopaminergic progenitor cells for Parkinson's disease, Nat. Commun. 11 (1) (2020) 3369.
[15] K. Sugai, M. Sumida, T. Shofuda, R. Yamaguchi, T. Tamura, T. Kohzuki, T. Abe, R. Shibata, Y. Kamata, S. Ito, T. Okubo, O. Tsuji, S. Nori, N. Nagoshi, S. Yamanaka, S. Kawamata, Y. Kanemura, M. Nakamura, H. Okano, First-in-human clinical trial of transplantation of iPSC-derived NS/PCs in subacute complete spinal cord injury: study protocol, Regen Ther 18 (2021) 321–333.
[16] H. Kamao, M. Mandai, S. Okamoto, N. Sakai, A. Suga, S. Sugita, J. Kiryu, M. Takahashi, Characterization of human induced pluripotent stem cell-derived retinal pigment epithelium cell sheets aiming for clinical application, Stem Cell Rep. 2 (2) (2014) 205–218.
[17] X. Duan, Q. Tu, J. Zhang, J. Ye, C. Sommer, G. Mostoslavsky, D. Kaplan, P. Yang, J. Chen, Application of induced pluripotent stem (iPS) cells in periodontal tissue regeneration, J. Cell. Physiol. 226 (1) (2011) 150–157.
[18] Y.S. Chen, R.A. Pelekanos, R.L. Ellis, R. Horne, E.J. Wolvetang, N.M. Fisk, Small molecule mesengenic induction of human induced pluripotent stem cells to generate mesenchymal stem/stromal cells, Stem Cells Transl Med 1 (2) (2012) 83–95.
[19] Q. Zhao, C.A. Gregory, R.H. Lee, R.L. Reger, L. Qin, B. Hai, M.S. Park, N. Yoon, B. Clough, E. McNeill, D.J. Prockop, F. Liu, MSCs derived from iPSCs with a modified protocol are tumor-tropic but have much less potential to promote tumors than bone marrow MSCs, Proc. Natl. Acad. Sci. U. S. A. 112 (2) (2015) 530–535.
[20] S. Mitsuzawa, C. Zhao, R. Ikeguchi, T. Aoyama, D. Kamiya, M. Ando, H. Takeuchi, S. Akieda, K. Nakayama, S. Matsuda, M. Ikeya, Pro-angiogenic scaffold-free Bio three-dimensional conduit developed from human induced pluripotent stem cell-derived mesenchymal stem cells promotes peripheral nerve regeneration, Sci. Rep. 10 (1) (2020) 12034.
[21] D. Kamiya, N. Takenaka-Ninagawa, S. Motoike, M. Kajiya, T. Akaboshi, C. Zhao, M. Shibata, S. Senda, Y. Toyooka, H. Sakurai, H. Kurihara, M. Ikeya, Induction of functional xeno-free MSCs from human iPSCs via a neural crest cell lineage, NPJ Regen Med 7 (1) (2022) 47.
[22] D. Zujur, Z. Al-Akashi, A. Nakamura, C. Zhao, K. Takahashi, S. Aritomi, W. Theoputra, D. Kamiya, K. Nakayama, M. Ikeya, Enhanced chondrogenic differentiation of iPS cell-derived mesenchymal stem/stromal cells via neural crest cell induction for hyaline cartilage repair, Front. Cell Dev. Biol. 11 (2023) 1140717.
[23] H. Egusa, H. Kayashima, J. Miura, S. Uraguchi, F. Wang, H. Okawa, J. Sasaki, M. Saeki, T. Matsumoto, H. Yatani, Comparative analysis of mouse-induced pluripotent stem cells and mesenchymal stem cells during osteogenic differentiation in vitro, Stem Cell. Dev. 23 (18) (2014) 2156–2169.
[24] J.Y. Ko, S. Park, G.I. Im, Osteogenesis from human induced pluripotent stem cells: an in vitro and in vivo comparison with mesenchymal stem cells, Stem Cell. Dev. 23 (15) (2014) 1788–1797.
[25] H. Ochiai-Shino, H. Kato, T. Sawada, S. Onodera, A. Saito, T. Takato, T. Shibahara, T. Muramatsu, T. Azuma, A novel strategy for enrichment and isolation of osteoprogenitor cells from induced pluripotent stem cells based on surface marker combination, PLoS One 9 (6) (2014) e99534.
[26] S. Diederichs, R.S. Tuan, Functional comparison of human-induced pluripotent stem cell-derived mesenchymal cells and bone marrow-derived mesenchymal stromal cells from the same donor, Stem Cell. Dev. 23 (14) (2014) 1594–1610.
[27] T. Sato, T. Anada, R. Hamai, Y. Shiwaku, K. Tsuchiya, S. Sakai, K. Baba, K. Sasaki, O. Suzuki, Culture of hybrid spheroids composed of calcium phosphate materials and mesenchymal stem cells on an oxygen-permeable culture device to predict in vivo bone forming capability, Acta Biomater. 88 (2019) 477–490.
[28] J. Ji, X. Tong, X. Huang, T. Wang, Z. Lin, Y. Cao, J. Zhang, L. Dong, H. Qin, Q. Hu, Sphere-shaped nano-hydroxyapatite/chitosan/gelatin 3D porous scaffolds increase proliferation and osteogenic differentiation of human induced pluripotent stem cells from gingival fibroblasts, Biomed. Mater. 10 (4) (2015) 045005.
[29] J. Ji, X. Tong, X. Huang, J. Zhang, H. Qin, Q. Hu, Patient-derived human induced pluripotent stem cells from gingival fibroblasts composited with defined nanohydroxyapatite/chitosan/gelatin porous scaffolds as potential bone graft substitutes, Stem Cells Transl Med 5 (1) (2016) 95–105.
[30] S.J. Lee, S.W. Kang, H.J. Do, I. Han, D.A. Shin, J.H. Kim, S.H. Lee, Enhancement of bone regeneration by gene delivery of BMP2/Runx2 bicistronic vector into adipose-derived stromal cells, Biomaterials 31 (21) (2010) 5652–5659.
[31] J. Fan, C.-S. Lee, S. Kim, X. Zhang, J. Pi-Anfruns, M. Guo, C. Chen, M. Rahnama, J. Li, B.M. Wu, T.L. Aghaloo, M. Lee, Trb3 controls mesenchymal stem cell lineage fate and enhances bone regeneration by scaffold-mediated local gene delivery, Biomaterials 264 (2021) 120445.
[32] A.G. Robling, L.F. Bonewald, The osteocyte: new insights, Annu. Rev. Physiol. 82 (2020) 485–506.
[33] H. Kitaura, A. Marahleh, F. Ohori, T. Noguchi, W.R. Shen, J. Qi, Y. Nara, A. Pramusita, R. Kinjo, I. Mizoguchi, Osteocyte-related cytokines regulate osteoclast formation and bone resorption, Int. J. Mol. Sci. 21 (14) (2020).
[34] X. Tu, J. Delgado-Calle, K.W. Condon, M. Maycas, H. Zhang, N. Carlesso, M. M. Taketo, D.B. Burr, L.I. Plotkin, T. Bellido, Osteocytes mediate the anabolic actions of canonical Wnt/β-catenin signaling in bone, Proc. Natl. Acad. Sci. U. S. A. 112 (5) (2015) E478–E486.
[35] X. Wang, Y. Ma, J. Chen, Y. Liu, G. Liu, P. Wang, B. Wang, M.M. Taketo, T. Bellido, X. Tu, A novel decellularized matrix of Wnt signaling-activated osteocytes accelerates the repair of critical-sized parietal bone defects with osteoclastogenesis, angiogenesis, and neurogenesis, Bioact. Mater. 21 (2023) 110–128.
[36] Y. Liu, X. Ruan, J. Li, B. Wang, J. Chen, X. Wang, P. Wang, X. Tu, The osteocyte stimulated by Wnt agonist SKL2001 is a safe osteogenic niche improving bioactivities in a polycaprolactone and cell integrated 3D module, Cells 11 (5) (2022).
[37] Y. Luo, Y. Liu, B. Wang, X. Tu, CHIR99021-Treated osteocytes with Wnt activation in 3D-printed module form an osteogenic microenvironment for enhanced osteogenesis and vasculogenesis, Int. J. Mol. Sci. 24 (6) (2023).
[38] P. Wang, X. Wang, B. Wang, X. Li, Z. Xie, J. Chen, T. Honjo, X. Tu, 3D printing of osteocytic Dll4 integrated with PCL for cell fate determination towards osteoblasts in vitro, Bio-Design and Manufacturing 5 (3) (2022) 497–511.
[39] M. Fukuta, Y. Nakai, K. Kirino, M. Nakagawa, K. Sekiguchi, S. Nagata, Y. Matsumoto, T. Yamamoto, K. Umeda, T. Heike, N. Okumura, N. Koizumi, T. Sato, T. Nakahata, M. Saito, T. Otsuka, S. Kinoshita, M. Ueno, M. Ikeya, J. Toguchida, Derivation of mesenchymal stromal cells from pluripotent stem cells through a neural crest lineage using small molecule compounds with defined media, PLoS One 9 (12) (2014) e112291.
[40] F.C. Gonsalves, K. Klein, B.B. Carson, S. Katz, L.A. Ekas, S. Evans, R. Nagourney, T. Cardozo, A.M. Brown, R. DasGupta, An RNAi-based chemical genetic screen identifies three small-molecule inhibitors of the Wnt/wingless signaling pathway, Proc. Natl. Acad. Sci. U. S. A. 108 (15) (2011) 5954–5963.
[41] L. Jia, X. Zhou, X. Huang, X. Xu, Y. Jia, Y. Wu, J. Yao, Y. Wu, K. Wang, Maternal and umbilical cord serum-derived exosomes enhance endothelial cell proliferation and migration, Faseb. J. 32 (8) (2018) 4534–4543.
[42] X. Tu, K.S. Joeng, K.I. Nakayama, K. Nakayama, J. Rajagopal, T.J. Carroll, A. P. McMahon, F. Long, Noncanonical Wnt signaling through G protein-linked PKCdelta activation promotes bone formation, Dev. Cell 12 (1) (2007) 113–127.
[43] C. Luzzani, G. Neiman, X. Garate, M. Questa, C. Solari, D. Fernandez Espinosa, M. García, A.L. Errecalde, A. Guberman, M.E. Scassa, G.E. Sevlever, L. Romorini, S.

G. Miriuka, A therapy-grade protocol for differentiation of pluripotent stem cells into mesenchymal stem cells using platelet lysate as supplement, Stem Cell Res. Ther. 6 (1) (2015) 6.
[44] P.W. Andrews, P.J. Gokhale, A short history of pluripotent stem cells markers, Stem Cell Rep. 19 (1) (2024) 1–10.
[45] K.G. Chen, K.R. Johnson, K. Park, D. Maric, F. Yang, W.F. Liu, Y.C. Fann, B. S. Mallon, P.G. Robey, Resistance to naïve and formative pluripotency conversion in RSeT human embryonic stem cells, bioRxiv (2024).
[46] C.E. Aban, A. Lombardi, G. Neiman, M.C. Biani, A. La Greca, A. Waisman, L. N. Moro, G. Sevlever, S. Miriuka, C. Luzzani, Downregulation of E-cadherin in pluripotent stem cells triggers partial EMT, Sci. Rep. 11 (1) (2021) 2048.
[47] H.F. Chen, C.Y. Chuang, W.C. Lee, H.P. Huang, H.C. Wu, H.N. Ho, Y.J. Chen, H. C. Kuo, Surface marker epithelial cell adhesion molecule and E-cadherin facilitate the identification and selection of induced pluripotent stem cells, Stem Cell Rev Rep 7 (3) (2011) 722–735.
[48] H. Ise, K. Matsunaga, M. Shinohara, Y. Sakai, Improved isolation of mesenchymal stem cells based on interactions between N-Acetylglucosamine-Bearing polymers and cell-surface Vimentin, Stem Cell. Int. 2019 (2019) 4341286.
[49] W.T. Lai, V. Krishnappa, D.G. Phinney, Fibroblast growth factor 2 (Fgf2) inhibits differentiation of mesenchymal stem cells by inducing Twist2 and Spry4, blocking extracellular regulated kinase activation, and altering Fgf receptor expression levels, Stem Cell. 29 (7) (2011) 1102–1111.
[50] C. Dumortier, S. Danopoulos, F. Velard, D. Al Alam, Bone cells differentiation: how CFTR mutations may rule the game of stem cells commitment? Front. Cell Dev. Biol. 9 (2021) 611921.
[51] R.H. Xu, T.L. Sampsell-Barron, F. Gu, S. Root, R.M. Peck, G. Pan, J. Yu, J. Antosiewicz-Bourget, S. Tian, R. Stewart, J.A. Thomson, NANOG is a direct target of TGFbeta/activin-mediated SMAD signaling in human ESCs, Cell Stem Cell 3 (2) (2008) 196–206.
[52] M. Wu, G. Chen, Y.P. Li, TGF-β and BMP signaling in osteoblast, skeletal development, and bone formation, homeostasis and disease, Bone Res 4 (2016) 16009.
[53] F. Gu, K. Zhang, J. Li, X. Xie, Q. Wen, Z. Sui, Z. Su, T. Yu, Changes of migration, immunoregulation and osteogenic differentiation of mesenchymal stem cells in different stages of inflammation, Int. J. Med. Sci. 19 (1) (2022) 25–33.
[54] A. Neve, A. Corrado, F.P. Cantatore, Osteocytes: central conductors of bone biology in normal and pathological conditions, Acta Physiol. 204 (3) (2012) 317–330.
[55] Y. Zhang, Y. Zhao, Z. Xie, M. Li, Y. Liu, X. Tu, Activating Wnt/β-catenin signaling in osteocytes promotes osteogenic differentiation of BMSCs through BMP-7, Int. J. Mol. Sci. 23 (24) (2022).
[56] G. Turnbull, J. Clarke, F. Picard, P. Riches, L. Jia, F. Han, B. Li, W. Shu, 3D bioactive composite scaffolds for bone tissue engineering, Bioact. Mater. 3 (3) (2018) 278–314.
[57] S. Ivanovski, O. Breik, D. Carluccio, J. Alayan, R. Staples, C. Vaquette, 3D printing for bone regeneration: challenges and opportunities for achieving predictability, Periodontol. 2000 93 (1) (2023) 358–384.
[58] O. Riester, M. Borgolte, R. Csuk, H.P. Deigner, Challenges in bone tissue regeneration: stem cell therapy, biofunctionality and antimicrobial properties of novel materials and its evolution, Int. J. Mol. Sci. 22 (1) (2020).
[59] V. Sabapathy, S. Kumar, hiPSC-derived iMSCs: NextGen MSCs as an advanced therapeutically active cell resource for regenerative medicine, J. Cell Mol. Med. 20 (8) (2016) 1571–1588.
[60] A. Mahmood, L. Harkness, H.D. Schrøder, B.M. Abdallah, M. Kassem, Enhanced differentiation of human embryonic stem cells to mesenchymal progenitors by inhibition of TGF-beta/activin/nodal signaling using SB-431542, J. Bone Miner. Res. 25 (6) (2010) 1216–1233.
[61] E. Sachlos, D.T. Auguste, Embryoid body morphology influences diffusive transport of inductive biochemicals: a strategy for stem cell differentiation, Biomaterials 29 (34) (2008) 4471–4480.
[62] R.L. Carpenedo, A.M. Bratt-Leal, R.A. Marklein, S.A. Seaman, N.J. Bowen, J. F. McDonald, T.C. McDevitt, Homogeneous and organized differentiation within embryoid bodies induced by microsphere-mediated delivery of small molecules, Biomaterials 30 (13) (2009) 2507–2515.
[63] K. Zeevaert, M.H. Elsafi Mabrouk, W. Wagner, R. Goetzke, Cell mechanics in embryoid bodies, Cells 9 (10) (2020).
[64] J.S. Morales, J. Raspopovic, L. Marcon, From embryos to embryoids: how external signals and self-organization drive embryonic development, Stem Cell Rep. 16 (5) (2021) 1039–1050.
[65] L. Sánchez, I. Gutierrez-Aranda, G. Ligero, R. Rubio, M. Muñoz-López, J.L. García-Pérez, V. Ramos, P.J. Real, C. Bueno, R. Rodríguez, M. Delgado, P. Menendez, Enrichment of human ESC-derived multipotent mesenchymal stem cells with immunosuppressive and anti-inflammatory properties capable to protect against experimental inflammatory bowel disease, Stem Cell. 29 (2) (2011) 251–262.
[66] K. Hynes, D. Menicanin, K. Mrozik, S. Gronthos, P.M. Bartold, Generation of functional mesenchymal stem cells from different induced pluripotent stem cell lines, Stem Cell. Dev. 23 (10) (2014) 1084–1096.
[67] Y. Jiang, P. Zhang, X. Zhang, L. Lv, Y. Zhou, Advances in mesenchymal stem cell transplantation for the treatment of osteoporosis, Cell Prolif. 54 (1) (2021) e12956.
[68] M.B. Schaffler, W.Y. Cheung, R. Majeska, O. Kennedy, Osteocytes: master orchestrators of bone, Calcif. Tissue Int. 94 (1) (2014) 5–24.
[69] J. Buckland, Bone: anabolic Wnt/β-catenin signalling: osteocytes are key, Nat. Rev. Rheumatol. 11 (3) (2015) 128.
[70] S. Stevenson, S.E. Emery, V.M. Goldberg, Factors affecting bone graft incorporation, Clin. Orthop. Relat. Res. 324 (1996) 66–74.
[71] O. Baru, A. Nutu, C. Braicu, C.A. Cismaru, I. Berindan-Neagoe, S. Buduru, M. Badea, Angiogenesis in regenerative dentistry: are we far enough for therapy? Int. J. Mol. Sci. 22 (2) (2021).
[72] X.D. Wang, S.Y. Li, S.J. Zhang, A. Gupta, C.P. Zhang, L. Wang, The neural system regulates bone homeostasis via mesenchymal stem cells: a translational approach, Theranostics 10 (11) (2020) 4839–4850.
[73] M.I. Santos, R.L. Reis, Vascularization in bone tissue engineering: physiology, current strategies, major hurdles and future challenges, Macromol. Biosci. 10 (1) (2010) 12–27.
[74] L. Krishnan, N.J. Willett, R.E. Guldberg, Vascularization strategies for bone regeneration, Ann. Biomed. Eng. 42 (2) (2014) 432–444.
[75] E. Mercado-Pagán Á, A.M. Stahl, Y. Shanjani, Y. Yang, Vascularization in bone tissue engineering constructs, Ann. Biomed. Eng. 43 (3) (2015) 718–729.
[76] W. Sun, B. Ye, S. Chen, L. Zeng, H. Lu, Y. Wan, Q. Gao, K. Chen, Y. Qu, B. Wu, X. Lv, X. Guo, Neuro-bone tissue engineering: emerging mechanisms, potential strategies, and current challenges, Bone Res 11 (1) (2023) 65.
[77] P.K. L, S. Kandoi, R. Misra, V. S, R. K, R.S. Verma, The mesenchymal stem cell secretome: a new paradigm towards cell-free therapeutic mode in regenerative medicine, Cytokine Growth Factor Rev. 46 (2019) 1–9.
[78] L. Neufeld, E. Yeini, S. Pozzi, R. Satchi-Fainaro, 3D bioprinted cancer models: from basic biology to drug development, Nat. Rev. Cancer 22 (12) (2022) 679–692.
[79] Z. Zhou, Y. Pang, J. Ji, J. He, T. Liu, L. Ouyang, W. Zhang, X.L. Zhang, Z.G. Zhang, K. Zhang, W. Sun, Harnessing 3D in vitro systems to model immune responses to solid tumours: a step towards improving and creating personalized immunotherapies, Nat. Rev. Immunol. 24 (1) (2024) 18–32.
[80] D. Wu, Z. Wang, J. Li, Y. Song, M.E.M. Perez, Z. Wang, X. Cao, C. Cao, S. Maharjan, K.C. Anderson, D. Chauhan, Y.S. Zhang, A 3D-bioprinted multiple myeloma model, Adv. Healthcare Mater. 11 (7) (2022) e2100884.